

## **Supplementary information to “Inherited terrane properties explain enigmatic post-collisional Himalayan-Tibetan evolution”**

Sean Kelly \*<sup>1</sup>, Christopher Beaumont<sup>2</sup>, and Jared P. Butler<sup>2,3</sup>

<sup>1</sup>Earth Science and <sup>2</sup>Oceanography Departments, Dalhousie University, Halifax, NS, Canada, B3H 4R2

<sup>3</sup> Now at Geological Survey of Newfoundland and Labrador, St. John's, NL, Canada, A1B 4J6

## **Testable Predictions**

### **Testable Predictions and Relationships Derived from Models MA and MB**

We derive the following testable predictions and relationships from MA and MB model results and comparison with observations. They are listed in chronological order. Times listed in Ma are approximate.

- 1) At 90°E contact between distal margins of Asia and Greater India was at ~11°N.
- 2) The rifted margin of Greater India was ~1000 km wide based on sedimentary contact, and was subducted northward between 58 and 52 Ma, leading to full continent–continent collision at 52 Ma. The width may have been less if the apron of sediment on the Greater Indian margin extended significantly onto Neotethys oceanic lithosphere.
- 3) Slab breakoff at 52 Ma was in the Greater India margin, and was followed by UHP exhumation at 50 Ma. Slab breakoff may explain the 51 Ma peak Gangdese arc magmatic flare up.
- 4) Lithospheric decoupling and widening of the subduction channel followed UHP exhumation. It allowed asthenospheric upwelling causing decompression melting and heating of overlying Tethyan Himalayan crust. This heating can explain Eo-Himalayan crustal magmatism and metamorphism.
- 5) Asthenospheric upwelling in, and adjacent to, the subduction channel at ~50 Ma may also be responsible for the Gangdese magmatic flare up.

- 6) After slab break-off, Indian lithosphere primarily indented Asia resulting in little growth of the Himalayan by accretion from India during the interval ~50–25 Ma.
- 7) Initial Indian indentation is accommodated primarily by shortening and delamination of the Qiangtang CLM. This leads to rapid northward translation of both the IYS suture and the Lhasa terrane.
- 8) Delamination of the Qiangtang CLM at ~44 Ma causes Qiangtang magmatism. The style and timing of delamination may vary resulting in diachroneity and differences in the amount of Qiangtang magmatism along strike.
- 9) Closure of the opening in the subduction channel at ~36 Ma explains termination of 50–38 Ma low-volume Linzizong magmatism.
- 10) Northward subduction of Lhasa terrane CLM follows Qiangtang CLM delamination. The style may be intracontinental subduction (MB) or double subduction followed by detachment and retreat (MA), while the overlying crust translates northward.
- 11) Progressive removal of Lhasa CLM and exposure of overlying crust to upwelling asthenosphere explains the 27–22 Ma southward sweep or jump of magmatism from the Qiangtang to south Lhasa terranes.
- 12) South Lhasa crust remains exposed to upwelled asthenosphere from 20–10 Ma, which leads to additional magmatism and significant heating of the lower/middle Lhasa crust.
- 13) Removal of Lhasa ( $\pm$  Songpan-Ganzi) CLM allows the initiation of Indian CLM underthrusting beneath the Lhasa crust at ~20 Ma. This underthrusting is responsible for renewed detachment and accretion of Indian crust and reactivation of thrusting in the vicinity of the IYS suture and on the Himalayan Main Central Thrust.
- 14) Indian CLM underthrusts Lhasa crust and contacts Songpan-Ganzi by ~10 Ma CLM causing south Lhasa magmatism to cease.
- 15) Onset of north Tibetan magmatism is partly explained by radioactive crustal incubation heating which spans ~ 20 Myr after crustal shortening and thickening.

16) Underthrust Indian CLM entrains the Kunlun CLM followed by delamination and curl-back of the combined CLM lump. Recent 3 Ma magmatism and hot xenoliths in Qiangtang crust can be explained by asthenospheric upwelling following delamination of this CLM lump.

17) Underthrusting of Indian CLM since 23–20 Ma amounts to ~500 km, in agreement with 400–670 km estimates of coeval shortening in the Himalaya.

18) Significant removal of Asian CLM by either subduction or delamination leads to loss of attached Asian lower crust. Although this missing lower crust may be replaced by Indian lower crust or magmatic underplating, regions of thin lower crust may remain under the Tibetan plateau.

19) Convergence of the IYS suture on stable Asia is much greater than current geological estimates of the shortening of Tibetan terranes if the 90°E contact between distal margins of Asia and Greater India was at ~11°N at 58 Ma.

### **Implications of Models MA and MB for Mantle Tomography Images**

While the models show general agreement with some tomographic images, uncertainties remain about the current state of the mantle under India and Tibet. We list predictions derived from MA and MB concerning the locations and nature of seismic tomographic anomalies.

1) At 90°E, the combined Neotethys and Indian margin slab is located at ~11°N. This corresponds to anomaly NT from Replumaz et al. (2013).

2) Delaminated Qiangtang CLM is located at ~27°N along 90°E. This corresponds to the tomographic anomaly AS from Replumaz et al. (2013) at 1000 km depth, 90°E.

3) Delaminated Lhasa CLM is also located at ~27°N along 90°E, albeit at shallower depth than the Qiangtang CLM. This corresponds to the 90°E tomographic anomaly 'IN' at 600 km depth and 25–28°N, above the AS anomaly. This is predicted to be Lhasa CLM, not Indian.

4) Entrained Indian/Kunlun CLM curls back to produce thick regions of CLM below the Lhasa terrane.

5) In other regions, no equivalent curled CLM lump is imaged and the slow velocity region to the north is missing. In these regions the delamination and curl back of the CLM lump is yet to happen.

### **Testable Predictions Reference**

Replumaz, A., Guillot, S., Villaseñor, A., and Negredo, A.M., 2013, Amount of Asian lithospheric mantle subducted during the India/Asia collision: *Gondwana Research*, v. 24, p. 936–945, doi.org/10.1016/j.gr.2012.07.019.

## **Recent Numerical Modelling Papers that Address Aspects of the Evolution of the Himalayan-Tibetan Orogen**

Burov and Yamato (2008) addresses the problem of deviations from lithostatic pressure in accreted and subsequently exhumed metamorphic rocks by numerical thermal-mechanical modeling of lithospheric simple shear (subduction), pure shear (collision), folding and Rayleigh-Taylor instabilities. Variations in Moho temperature and convergence velocity are tested. Their results indicate near normal pressures in the subduction channel but large-scale zones of tectonic overpressure outside the channel. However, these do not affect the exhumed rocks. The results support the interpretation that UHP rocks are exhumed from deep in the lithosphere. The same mechanism is seen in models MA and MB.

Burov, E., and Yamato, P., 2008, Continental plate collision, P-T-t-z conditions and unstable vs. stable plate dynamics: Insights from thermo-mechanical modelling: *Lithos*, v. 103, p. 178-204, doi:10.1016/j.lithos.2007.09.014.

Chen et al. (2017) uses 3D numerical models to examine the effects of crustal rheology on the formation of the Himalayan-Tibetan orogenic system. They show that deformation and plateau development focuses in weaker crust far into the interior of the upper (Asian) plate, whereas stronger crust suppresses plateau formation. It is concluded that crustal strength heterogeneity controls lithospheric deformation of the Asian continental crust. We agree that crustal heterogeneity may play a role but Chen et al. (2017) present little about the behavior of the mantle lithosphere so that its role in convective removal, delamination and other styles of

deformation, and associated magmatism, is not addressed. We suggest that lithospheric mantle heterogeneity is the main determinant of Himalayan-Tibetan orogenesis.

Chen, L., Capitanio, F.A., Liu, L., and Gerya, T.V., 2017, Crustal rheology controls on the Tibetan plateau formation during India-Asia convergence: *Nature Communications*, v. 8, 15992, doi: 10.1038/ncomms15992.

Copley et al. (2011) model active stress and faulting in the Tibetan plateau crust to show that the difference between strike-slip faulting in the northern plateau and normal faulting in southern Tibet requires mechanical coupling between the upper crust in southern Tibet and the underthrusting Indian crust. They conclude such coupling is inconsistent with active channel flow beneath southern Tibet. Only three end-member models are considered, so it is not clear whether a ~ 25 km thick mid-crustal channel region with a viscosity of  $10^{19}$  Pa.s would transmit sufficient shear stress to give normal faulting in the model in southern Tibet. Nor is the possible effect of 'patchy' weak mid-crust investigated. Models MA and MB develop hot weak regions in the thick mid-crust beneath the plateau region which undergo limited channel flow. The system remains coupled to the degree that underthrusting of the Indian lower crust and mantle lithosphere continues to advect overlying Asian crust to the north.

Copley, A., Avouac, J.-P., and Wernicke, B. P., 2011, Evidence for mechanical coupling and strong Indian lower crust beneath southern Tibet: *Nature*, v. 472, p.79-81, doi:10.1038/nature09926.

Koulakov et al. (2018) uses 2D thermomechanical numerical modelling to support the interpretation that earthquakes in India, far from the active plate boundary, correspond to the initiation of deformation which has been transferred from high mountain areas to a weak zone in the Indian lithosphere. The model results are relevant to our study in that the effects of thick and thin lithospheric regions are investigated. The model results show systematic migration of deformation from the weak to strong domains, which tend to underthrust the weak regions. However, their progressive development of the H-T orogen contrasts with Models MA and MB.

Koulakov, I., Gerya, T., Rastogi, B.K., Jakovlev, A., Medved, I., Kayal, J.R., El Khrepy, S., and Al-Arifi, N., 2018, Growth of mountain belts in central Asia triggers a new collision zone in central India: *Scientific Reports*, v. 8, 10710, doi:10.1038/s41598-018

29105-2.

Li, Z.H., Liu, M., and Gerya, T., 2016, Lithosphere delamination in continental collisional orogens: A systematic numerical study: *Journal of Geophysical Research*, v.121, p. 5186-5211. This paper is referenced and discussed in the main text.

Liao and Gerya (2017) uses 2D thermomechanical numerical modelling to investigate the effects of upper crustal strength, Moho temperature and convergence rate on partitioning of deformation between lower and upper plates during continental collision. Their results favor upper plate deformation when the lower plate has a strong upper crust, there is a high Moho temperature, and a slow convergence rate. These results are generally comparable to ours. We, like Kelly et al. (2016) find that a strong lower plate mantle, moderate Moho temperatures and even rapid convergence result in upper plate (Asian) deformation when models contain relatively weak Asian terranes.

Liao, J., and Gerya, T., 2017, Partitioning of crustal shortening during continental collision: 2-D thermomechanical modeling: *Journal of Geophysical Research Solid Earth*, v.122, p. 592-606, doi:10.1002/2016JB013398.

Kelly, S., Butler, J. P., and Beaumont, C., 2016, Continental collision with a sandwiched accreted terrane: Insights into Himalayan–Tibetan lithospheric mantle tectonics?: *Earth and Planetary Science Letters*, v. 455, p. 176–195, doi.org/10.1016/j.epsl.2016.08.039. This paper is referenced and discussed in the main text.

Pang et al. (2018) uses 3D thermomechanical numerical models to investigate N-S trending rifts in the Tibetan plateau. The models have velocity boundary conditions that cause N-S shortening and E-W extension. Models with a weak mid- to lower crust reproduce the N-S rifts, whereas stronger lower crust produces strike-slip faulting. Taken at face value these results appear to be the opposite of those reported by Copley et al. (2011) (see above). However, the Pang et al. (2018) modelling does involve our complexity number 12 (Fig. 1 caption) which cannot be addressed with 2D cross-sectional models.

Pang, Y., Zhang, H., Gerya, T.V., Liao, J., Cheng, H., Shi, Y., 2018, The mechanism and dynamics of N-S rifting in Southern Tibet: Insight from 3-D thermomechanical modeling: *Journal of Geophysical Research; Solid Earth*, v.123, p. 859-877, doi.org/10.1002/2017JB014011.

Pusok and Kaus (2015) investigates the roles of subduction, collision and indentation on convergent margin lithospheric dynamics leading to the formation of plateaus in the upper plate. The results show that slab-pull alone does not form plateaus. There needs to be additional compressional lithospheric tectonic forces bolstered by strong retaining lithospheric blocks (e.g. Tarim terrane). Scaling analysis is used to identify four regimes of surface expression during continental collision, in which the Himalayan-Tibetan orogeny belongs to regime iv.

Pusok, A. E., and Kaus, B. J. P., 2015, Development of topography in 3-D continental-collision models: *Geochemistry, Geophysics, Geosystems*, v. 16, p. 1378-1400, doi:10.1002/2015GC005732.

## Methods

### Overview of SOPALE Nested Code

The numerical geodynamical models were computed using the 2D ALE thermomechanical finite-element (FE) software SOPALE-nested (Fullsack, 1995; Beaumont et al., 2009; Butler et al., 2014). Models are designed based on a simple geometry representing oceanic subduction followed by continent-continent collision in which one continent contains five already accreted terranes (Fig. 2). The methodology remains similar to our recent work (Beaumont et al., 2009; Butler et al., 2014; Kelly et al., 2016).

The models are computed by solving the equations for incompressible creeping (Stokes) flows (Eqs. M.1 and M.2) and energy balance (Eq. M.3) on an Eulerian grid subject to mechanical and thermal boundary conditions:

$$(M.1) \quad \frac{\partial \sigma_{ij}}{\partial x_i} - \frac{\partial P}{\partial x_j} + \rho g = 0, \quad i, j = 1, 2$$

$$(M.2) \quad \frac{\partial v_i}{\partial x_i} = 0, \quad i = 1, 2$$

$$(M.3) \quad \rho(T)c_p \left( \frac{\partial T}{\partial t} + v_i \frac{\partial T}{\partial x_i} \right) = \frac{\partial}{\partial x_i} K(T) \frac{\partial T}{\partial x_i} + A_R + A_{SH} + v_2 \alpha g T \rho(T), \quad i = 1, 2,$$

where  $\sigma_{ij}$  is the deviatoric stress tensor,  $x_i$  spatial coordinates,  $P$  pressure (mean stress),  $\rho$  density,  $g$  gravitational acceleration,  $v_i$  a component of velocity,  $c_p$  specific heat,  $T$  temperature,  $t$  time,  $K$  thermal conductivity,  $A_R$  crustal radioactive heat production per unit volume,  $A_{SH}$  shear heating, and  $\alpha$  volumetric thermal expansion. Coupling of the mechanical and thermal solutions is

achieved through the advection of radioactive crust, shear heating, thermal activation of viscous flow, and buoyancy forces arising from metamorphic phase changes and thermal expansion.

The models use a sub-grid approach in which a higher-resolution Eulerian computational domain is ‘nested’ within a larger, lower-resolution Eulerian domain. The velocity and thermal solution is first obtained for the full domain. This solution is then interpolated onto the boundaries of the nested domain encompassing the vicinity of the subduction zone and the accreted terranes. The computation is then repeated on the higher resolution grid. Coupling of the grids is maintained by using a single Lagrangian grid and cloud of tracking particles, which is passed between the two solutions, with the particles within the nested domain always obeying the higher resolution solution. The Lagrangian grid and particles are advected by the incremental displacement field each time step and they progressively accumulate the total model displacement and deformation and advection of the temperature field.

### **Model Geometry and Boundary Conditions**

The Eulerian model grid is 4000 km wide by 1200 km deep. The initial configuration of the Lagrangian model (Fig. 2) is 11350 km wide by 1200 km deep. This means that much of the Lagrangian grid is outside of the Eulerian computational grid but is progressively translated into the Eulerian grid by the boundary velocities. We also make use of the ALE (Arbitrary Lagrangian-Eulerian) nature of SOPALE which allows the Lagrangian grid to be translated with respect to the Eulerian grid by an externally imposed uniform velocity. This ‘panning’ process is used to move the retro-part of the Lagrangian grid into the Eulerian grid as deformation propagates through the retrolithosphere. This ensures that any part of the model that is currently deforming is within the Eulerian computational grid.

The starting geometry of the H-T system (Fig. 2a; Table DR1) is a simplification of the natural equivalent but contains the main components of the system, particularly estimated pre-collisional widths and properties of the previously accreted retrocontinent terranes and the Indian side of the system. The width of the retrocontinent is restored based on assumed Neotethys (NT) breakoff at 11°N at 90°E. This implies an increase in width of the retrocontinent of ~ 2200 km with respect to the current configuration, which is achieved by proportional increases in the lengths of the terranes south of the Tarim terrane. This approach is simple and avoids biasing the model geometry by observed estimates of the shortening of the individual terranes. We do not

include prior deformation of the Asian terranes which remains poorly understood, although there was certainly some deformation. Each lithospheric region is labelled with an abbreviation derived from the natural setting, thereby distinguishing models from observations but allowing easy comparison. Model properties (Fig. 2; Table DR1) are described in more detail below.

Differences in the depletion density (i.e., decrease in density with respect to sublithospheric mantle) of continental lithospheric mantle (CLM) may be interpreted to measure varying amounts of chemical depletion (e.g., as reflected in the Mg#). We explore retrolithosphere CLMs with variable depletion densities (Table DR1). The prolithosphere CLM has a constant depletion density of  $50 \text{ kg/m}^3$ . Models with significantly higher density (e.g., a depletion density of  $40 \text{ kg/m}^3$  or less) fail to produce indentation or advancing subduction, a crucial requirement for H-T orogenesis.

Subduction is initiated by a weak seed embedded between the NT oceanic lithosphere and the L-terrane which spans the entire lithosphere. Models have stress-free boundary conditions at the upper surface, and respectively free-slip and no-slip boundary conditions at the base and sides of the model. Total convergence of 4000 km over 58 Myr is based on mean convergence from Ingalls et al. (2017). The left lithospheric velocity boundary condition varies from  $V_p = 15\text{--}4.5 \text{ cm/yr}$  (Fig. 2) to reproduce the slowing convergence rate of the Indian plate after collision. The right lithospheric boundary condition has  $V_r = 0$  until the last 15 Myr of convergence, when it increases to  $1 \text{ cm/yr}$ , thereby allowing for 150 km of late convergence in the Tien Shan, which is outside of the model domain and not computed. Small sublithospheric boundary fluxes are used to ‘pump’ material out of the sides of the model to conserve volume and maintain isostatic equilibrium.

The continents have laterally uniform crustal radioactive heat production ( $A_R$ ) for the upper/middle, and lower continental crust of  $2.0$  and  $0.4 \text{ } \mu\text{W/m}^3$ , respectively. Coupled with the thermal boundary conditions, basal heat flux  $21 \text{ mW/m}^2$ , and no-flux side boundaries, the resulting initial steady state surface heat flow and Moho temperatures on the continents are  $74 \text{ mW/m}^2$  and  $\sim 650^\circ\text{C}$ . The steady state initial base-lithosphere temperature is  $\sim 1370^\circ\text{C}$  everywhere in the model. Material thermal expansivity ( $\alpha$ ) and conductivity ( $K$ ) are temperature-dependent, with values varying linearly (e.g., from  $K_1$  to  $K_2$ ) over a range of temperatures (e.g.,  $T_1$  to  $T_2$ ), as described in Table DR1. Other thermal properties are given in Table DR1.

## Material Properties

The flow laws and material properties are similar to those used in Beaumont et al. (2001) and Butler et al. (2013). For a more detailed justification for the choice of flow laws and the scaling of these flow laws see Butler et al. (2014). The parameters of the models are considered typical of continental and oceanic lithospheric materials (Beaumont et al., 2006, and refs. therein).

Model materials deform by either frictional-plastic (brittle) or viscous (ductile) flow that includes additional strain-softening/strain-weakening mechanisms. Brittle deformation is modeled using the frictional-plastic Drucker-Prager yield criterion,  $\sigma_y$ :

$$(M.4) \quad \sigma_y = (J'_2)^{1/2} = P \sin \phi_{\text{eff}} + C \cos \phi_{\text{eff}}$$

where  $J'_2$  is the second invariant of the deviatoric stress,  $P$  dynamical pressure (mean stress), and  $C$  cohesion. The effective angle of internal friction,  $\phi_{\text{eff}}$  is defined to include the effects of near-hydrostatic pore fluid pressure. The friction angle of all materials, except oceanic sediment, is decreased linearly from  $\phi_{\text{eff}} = 15^\circ$  (initial friction angle) to  $2^\circ$  (strain-softened value) as the effective strain increases from 0.5 to 1.5 (Table 1). Oceanic sediment has  $\phi_{\text{eff}} = 8-2^\circ$ .

Ductile deformation is modeled using power-law flow, for which the effective viscosity is:

$$(M.5) \quad \eta_{\text{eff}}^v = \frac{f}{W_s} A^{-1/n} I_2'^{(1-n/2n)} \exp\left(\frac{Q+PV}{nRT_K}\right)$$

where  $f$  is a viscosity scaling factor,  $W_s$  a strain-weakening factor,  $A$  the pre-exponential factor converted to the tensor invariant form,  $I_2'$  the second invariant of the deviatoric strain rate,  $n$  the stress exponent,  $Q$  activation energy,  $P$  pressure,  $V$  the activation volume for power-law creep,  $T_K$  absolute temperature, and  $R$  the universal gas constant. The scaling factor  $f$  allows us to model stronger and weaker materials than the laboratory-derived flow law in a predictable way. This scaling may be interpreted as dehydrated or hydrated rock types, or slightly different compositions.

For simplicity, we base the model materials on a small set of laboratory-determined flow laws. Continental upper/middle-crust and sediment rheologies are based on a wet quartzite flow-law ( $WQ \times f$ , Gleason and Tullis, 1995), lower-crustal and oceanic crustal rheologies are based on a dry Maryland diabase flow law ( $DMD \times f$ , where  $f = 0.1$ , Mackwell et al., 1998), and mantle rheologies are based on a wet olivine flow-law ( $WOL \times f$ , Karato and Wu, 1993) (Table 1).

Crustal materials viscously strain-weaken according to  $W_s$ , the strain-weakening factor (equation M.5), which varies linearly from 1 to 3 as the effective strain increases from 5 to 10.

When stress levels are high in the lithospheric mantle they are subject to a high stress limit, the Peierls stress (Katayama and Karato, 2008) by rescaling the effective viscosity by the Peierls weakening factor so that the stress is close to, but not less than, the Peierls threshold stress,  $\sigma_p$  (Table DR1). This is an approximation to the rapid decrease in effective viscosity that materials experience under an exponential flow law beyond the Peierls threshold stress.

Each crustal unit comprises an upper/middle crust with  $\phi_{\text{eff}}$  (hereafter simply  $\phi$ ) =  $15-2^\circ$  (except where noted), and a scaled wet quartzite (WQ $\times f$ ) flow law (Gleason and Tullis, 1995), overlying a lower crust with  $\phi = 15-2^\circ$  (where  $\phi = 2^\circ$  is fully strain-softened) and a dry Maryland diabase (DMD $\times 0.1$ ) flow law (Mackwell et al., 1998), scaled to represent intermediate granulite. The continents and accreted terranes have WQ $\times 1$  upper crusts, except for I-crust which has WQ $\times 1.25$ . The underlying CLM has  $\phi = 15-2^\circ$  and scaled wet olivine flow laws (WOL $\times f$ ; Karato and Wu, 1993) and overlies sublithospheric upper mantle (WOL $\times 2$ ) that extends to 660 km. For the pro-continent (I) and retro-continent (T), the CLM has WOL $\times 5$ , corresponding to cratonic properties. The  $f$ -scaling of the CLM of the accreted terranes varies among the model experiments (Fig. 2d), with the values for the MA model shown in Figure 2a. Owing to considerable uncertainty concerning the rheology of the lower mantle (Billen, 2010), we assume that the lower mantle has a uniform and constant viscosity of  $1 \times 10^{21}$  Pa s.

Sediment and upper/middle continental crust undergo melt-weakening in a similar temperature- and pressure-dependent manner as in Butler et al. (2015). The viscosity decreases linearly (representing the effect of a small, 4–7 per cent, partial melt) from the calculated power-law value to a fixed linear value of  $10^{19}$  Pa s over the range from the pressure-dependent dry solidus to the solidus temperature plus  $50^\circ\text{C}$ . The dry solidus is defined by P-T line segments joining the points ( $680^\circ\text{C}$ , 0 GPa), ( $900^\circ\text{C}$ , 2.8 GPa), and ( $1437^\circ\text{C}$ , 15 GPa) (Zheng et al. 2011). This fixed  $10^{19}$  Pa s viscosity is maintained at higher temperatures except for coesite-eclogite which develops restite properties if it exceeds P-T conditions defined by the line joining points ( $1000^\circ\text{C}$ , 2.87 GPa) and ( $1700^\circ\text{C}$ , 12.67 GPa). Overall, melt weakening is a secondary effect which enhances the decoupling between the mid- and lower crust and leads to channel flow in the retrolithosphere.

## Density, Volume and Mass Conservation During Phase Transitions

Crustal materials undergo reversible pressure- and temperature-dependent density changes corresponding to the eclogite and coesite-eclogite phase transitions following Warren et al. (2008) (see Table DR1 for density changes). In addition, sediment and upper/middle crust coesite-eclogite materials that achieve restite conditions (Butler et al., 2015) undergo an increase in  $f$  to 10 in the power-law viscosity to represent the formation of dry restite after melt extraction (Massonne and Fockenberg, 2012). Restite may subsequently revert to high-pressure eclogite densities, but does not further retrograde to reference crustal density.

Mantle materials undergo a reversible phase change at the upper-lower mantle boundary (~660 km depth) corresponding to the transformation of olivine to perovskite. The latter transformation is determined by a reaction with a Clapeyron slope of -2.0 MPa/K and results in a density increase (proportional for all mantle materials) of ~8% (for a discussion of these parameters, see Billen, 2010). Crustal materials undergo equivalent phase changes at the upper-lower mantle boundary. For simplicity, the models do not include the transformation of olivine to ringwoodite in the mantle transition zone (~440–660 km).

During these phase changes the incompressibility equation is modified to that of mass conservation:  $\partial \rho / \partial t = -\partial (\rho v_i) / \partial x_i$ . This accounts for the volume change and its effect on the buoyancy and velocity field. The volume change is calculated numerically by applying additional normal, compressive/dilatational forces to finite elements at the time they are subject to phase-related density changes. The value of the excess/reduced pressure is  $\Delta P = \Delta \rho / \beta_v \rho$ , where  $\beta_v$  is the viscous bulk modulus of the material, and  $\Delta \rho / \rho$  is the fractional change in density corresponding to the phase change. The excess/reduced pressure compresses/dilates material locally and only during the model time steps when the phase changes occur, thereby ensuring mass conservation. The fractional volume change accompanying a phase change is small in these models and its effect on the velocity field is minor because it only applies at the time of the phase change. However, failure to ensure mass conservation would have a long-term effect on the model because the buoyancy forces will be over- or under-estimated by the fractional error in the material volume.

## Surface Processes

The models have an upper free surface and the model topography is a product of the model calculation without any imposed constraints except for water loading where the surface is below sea level. Slope-dependent surface erosion acts on the local subaerial topography (Fig. 2). It varies according to local slope of the model surface, where it is defined by a maximum erosion rate  $E(x)$  that operates on a slope of  $45^\circ$  and is scaled down linearly to the local slope of the surface. The erosion rate is also modulated by a spatial climate function (Fig. 2) designed to reproduce wet (moderate erosion) conditions on the left-facing orogenic front and dry (lower erosion) conditions over the interior plateau region. The climate function tracks the development and movement of the orogen. Maximum erosion rates are  $\sim 0.5$  cm/yr on the orogenic front.

## Methods References

- Beaumont, C., Jamieson, R.A., Butler, J.P., and Warren, C.J., 2009, Crustal structure: A key constraint on the mechanism of ultra-high-pressure rock exhumation: *Earth and Planetary Science Letters*, v. 287, p. 116–129, doi:10.1016/j.epsl.2009.08.001.
- Beaumont, C., Nguyen, M.H., Jamieson, R.A. and Ellis, S., 2006, Crustal flow modes in large hot orogens: *in* Law, R.D., Searle, M.P., and Godin, L., eds., *Channel Flow, Ductile Extrusion, and Exhumation of Lower-Midcrust in Continental Collision Zones*: Geological Society [London] Special Publication 268, p.91–145.
- Beaumont, C., Jamieson, R.A., Nguyen, M.H., and Lee, B., 2001, Himalayan tectonics explained by extrusion of a low-viscosity crustal channel coupled to focused surface denudation: *Nature*, v. 414, p. 738–742.
- Billen, M.I., 2010, Slab dynamics in the transition zone: *Physics of the Earth and Planetary Interiors*, v.183, p. 296–308, doi:10.1016/j.pepi.2010.05.005.2010.
- Butler, J.P., Beaumont, C., and Jamieson, R.A., 2015, Paradigm lost: Buoyancy thwarted by the strength of the Western Gneiss Region (ultra) high-pressure terrane, Norway: *Lithosphere*, v. 7, p. 379–407, doi.org/10.1130/1426.1.
- Butler, J.P., Beaumont, C., and Jamieson, R.A., 2014, The Alps 2: Controls on crustal subduction and (ultra) high pressure rock exhumation in Alpine-type orogens. *Journal of Geophysical Research*, v. 119, p. 5987–6022, doi:10.1002/2013JB010799.
- Butler, J.P., Beaumont, C., and Jamieson, R.A., 2013, The Alps 1: A working geodynamic

- model for burial and exhumation of (ultra) high pressure rocks in Alpine-type orogens: *Earth and Planetary Science Letters*, v. 377-378, p. 114-131, doi:10.1016/j.epsl.2013.06.039.
- Fullsack, P., 1995, An arbitrary Lagrangian-Eulerian formulation for creeping flows and its application in tectonic models: *Geophysical Journal International*, v. 120, p.1-23.
- Gleason, G.C., and Tullis, J., 1995, A flow law for dislocation creep of quartz aggregates determined with the molten salt cell: *Tectonophysics*, v. 247, p.1–23.
- Ingalls, M., Rowley, D.B., Currie, B., and Colman. A.S., 2016, Large-scale subduction of continental crust implied by India–Asia mass-balance calculation: *Nature Geoscience*, v. 9, p. 848-853, doi:10.1038/NGEO2806.
- Karato, S.-I., and Wu P., 1993. Rheology of the upper mantle: A synthesis: *Science*, v. 260, p. 771–778.
- Katayama, I., and Karato, S-i., 2008, Low-temperature, high-stress deformation of olivine under water-saturated conditions: *Physics of the Earth and Planetary Interiors*, v. 168, p. 125–133, doi:10.1016/j.pepi.2008.05.019.
- Kelly, S., Butler, J.P., and Beaumont, C., 2016, Continental collision with a sandwiched accreted terrane: Insights into Himalayan–Tibetan lithospheric mantle tectonics?: *Earth and Planetary Science Letters*, v. 455, p. 176–195, doi.org/10.1016/j.epsl.2016.08.039.
- Mackwell, S., Zimmerman, M., and Kohlstedt, D., 1998, High-temperature deformation of dry diabase with application to tectonics on Venus: *Journal of Geophysical Research*, v. 103, p. 975–984, doi:10.1029/97JB02671.
- Massonne, H.-J., and Fockenberg, T., 2012, Melting of metasedimentary rocks at ultrahigh pressure-insights from experiments and thermodynamic calculations: *Lithosphere* v. 4, p. 269–285, doi: 10.1130/L185.1.
- Warren, C.J., Beaumont, C., and Jamieson, R.A., 2008, Modelling tectonic styles and ultrahigh pressure (UHP) rock exhumation during the transition from oceanic subduction to continental collision: *Earth and Planetary Science Letters*, v. 267, p.129–145.
- Zheng, Y-F., Xia, Q-X., Chen, R-X., and Gao, X-Y., 2011, Partial melting, fluid supercriticality and element mobility in ultrahigh-pressure metamorphic rocks during continental collision: *Earth-Science Reviews*, v.107, p. 342–374, doi.org/10.1016/j.earscirev.2011.04.004.

**Table DR1: Model Mechanical and Thermal parameters.**

The Table lists reference (constant) properties for oceanic, and pro- and retro- model regions (labelled P and R). The densities and  $f$ -scaling factors are for the reference properties. The density for pro-CLM,  $3320 \text{ kg m}^{-3}$ , corresponds to a depletion density of  $50 \text{ kg m}^{-3}$  with respect to sublithospheric upper mantle. These properties are varied for the retrolithospheric terranes in the model experiments as shown in Figure 2 where densities are given in terms of depletion density.

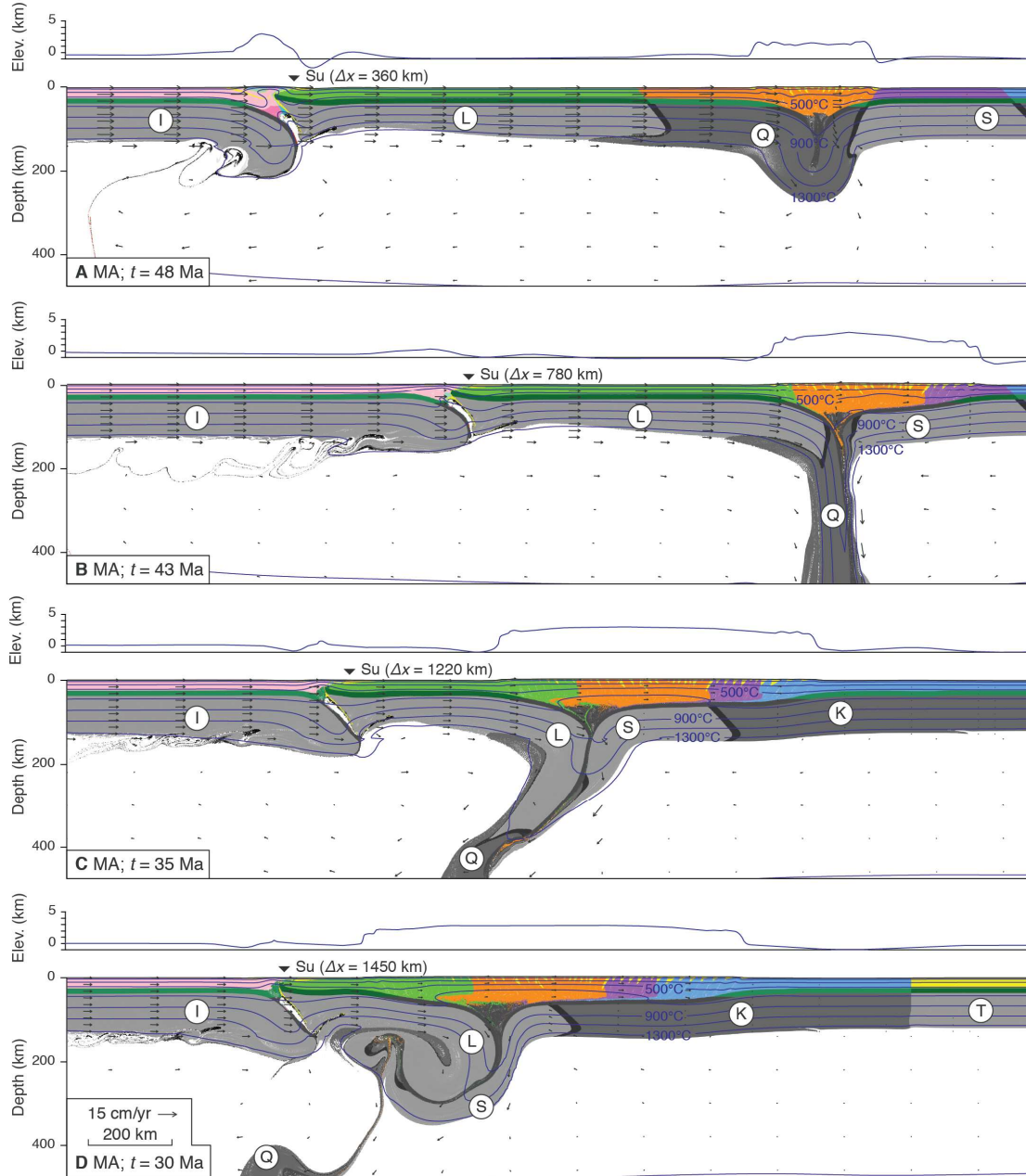
	Units	Oceanic Cover	Upper crust (PC and RC)	lower crust (PC and RC)	Oceanic crust	Continental lithospheric mantle (PC and RC)	Oceanic lithospheric mantle	Sub-lithospheric upper mantle	Lower mantle
Thickness (max)	km	2	24	12	6	84	92	To 660 km depth	660 to 1200 km depth
Reference density (0°C)	$\text{kg m}^{-3}$	2700	2700	2900	2950	Varies, see Fig. 2	$3370^\dagger$	3370	3630
Reference density HP (0°C) <sup>§</sup>	$\text{kg m}^{-3}$	2800	2950	3300	3400	No change	No change	No change	No change
Reference density UHP (0°C) <sup>§</sup>	$\text{kg m}^{-3}$	2900	3200	No change	No change	Increases from reference density by 260 below 660 km depth	Changes to 3630 below 660 km depth	Changes to 3630 below 660 km depth	No change
Effective angle of internal friction ( $\varphi_{eff}$ )	deg	8-2 <sup>#</sup>	15-2 <sup>#</sup>	15-2 <sup>#</sup>	15-2 <sup>#</sup>	15-2 <sup>#</sup>	15-2 <sup>#</sup>	15-2 <sup>#</sup>	15-2 <sup>#</sup>
Cohesion	MPa	2	2	2	0	0	0	0	0
Flow law	-	WQ	WQ	DMD	DMD	WOL	WOL	WOL	Constant viscosity $1 \times 10^{21} \text{ Pa s}$
Viscosity scaling factor ( $f$ )	-	1	Varies, see Fig. 2	0.1	0.1	Varies, see Fig. 2	2	2	-
Strain weakening factor ( $W_s$ )	-	3	3	3	3	1	1	1	-
$n$	-	4	4	4.7	4.7	3	3	3	-
$A^{\ddagger\dagger}$	$\text{Pa}^{-n} \text{ s}^{-1}$	$8.57 \times 10^{-28}$	$8.57 \times 10^{-28}$	$5.78 \times 10^{-27}$	$5.78 \times 10^{-27}$	$1.76 \times 10^{-14}$	$1.76 \times 10^{-14}$	$1.76 \times 10^{-14}$	-
$Q$	$\text{kJ mol}^{-1}$	223	223	485	485	430	430	430	-
$V^\circ$	$\text{m}^3 \text{ mol}^{-1}$	0	0	0	0	$11 \times 10^{-6}$	$11 \times 10^{-6}$	0	-
Peierls stress	MPa	-	-	-	-	100 (PC), 350 (RC)	150	-	-
Peierls weakening factor	-	-	-	-	-	$1 \times 10^{-5}$	$1 \times 10^{-5}$	-	-
Specific heat	$\text{m}^2 \text{ s}^{-2} \text{ K}^{-1}$	750	750	750	750	1250	1250	1250	1250
Thermal conductivity	$\text{W m}^{-1} \text{ K}^{-1}$	2.25	2.25	2.25	2.25	5-2.4 <sup>§§</sup>	5-2.4 <sup>§§</sup>	2.4-52.5 <sup>§§,##</sup>	2.4-52.5 <sup>§§,##</sup>
Thermal diffusivity	$\text{m}^2 \text{ s}^{-1}$	$1 \times 10^{-6}$	$1 \times 10^{-6}$	$1 \times 10^{-6}$	$1 \times 10^{-6}$	$1.3-0.64 \times 10^{-6} \text{ §§}$	$1.3-0.64 \times 10^{-6} \text{ §§}$	$0.64-14 \times 10^{-6} \text{ §§}$	$0.64-14 \times 10^{-6} \text{ §§}$
Thermal expansion coefficient	$\text{K}^{-1}$	$3 \times 10^{-5}$	$3 \times 10^{-5}$	$3 \times 10^{-5}$	$3 \times 10^{-5}$	$3.2-3.9 \times 10^{-5} \text{ †††}$	$3.2-3.9 \times 10^{-5} \text{ †††}$	$3.2-3.9 \times 10^{-5} \text{ †††}$	$3.2-3.9 \times 10^{-5} \text{ †††}$
Radioactive heat production	$\mu\text{W m}^{-3}$	1	2	0.4	0	0	0	0	0

<sup>†</sup> Oceanic lithospheric mantle is depleted by  $15 \text{ kg m}^{-3}$  above a depth of 60 km.

<sup>§</sup> High-pressure (HP) and ultrahigh-pressure (UHP) densities.

# Includes the effect of strain softening.  $\phi_{eff}$  varies from 15 to 2, or 8 to 2, as the accumulated effective strain increases from 0.5 to 1.5.  
 †† Experimental pre-exponential factor has been converted from laboratory value to a corresponding one written in terms of the second invariants of deviatoric stress and strain rate. This is required to ensure that the flow law is coordinate invariant.  
 §§ Thermal conductivity and diffusivity for lithospheric mantles vary linearly over the temperature range 273–1050 K.  
 ## Enhanced thermal conductivity and diffusivity required to maintain adiabatic temperature gradient of 0.4 K km<sup>-1</sup>.  
 ††† Thermal expansion coefficient increases linearly over the temperature range 500–2000 K.

## Supplementary Figures



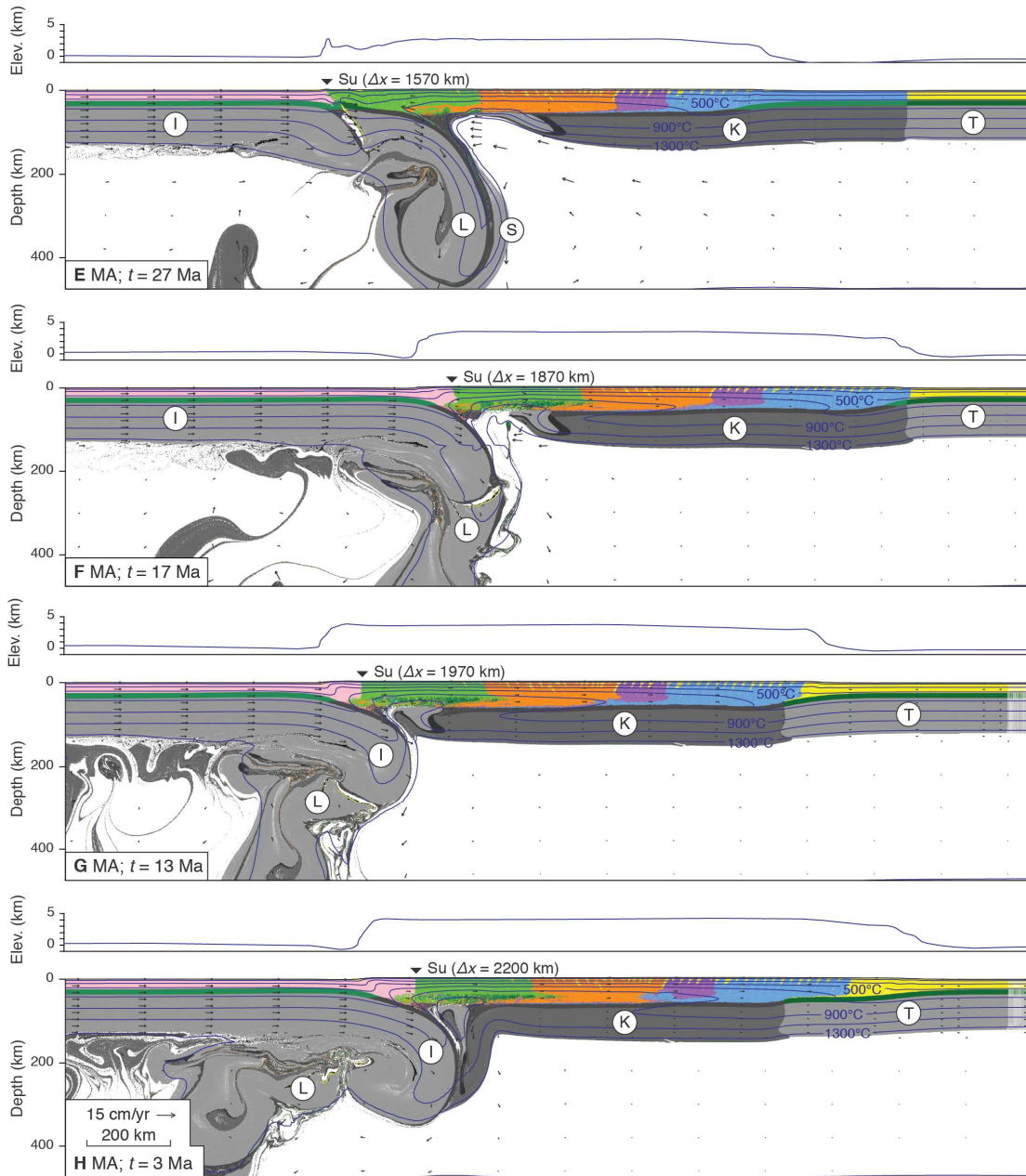
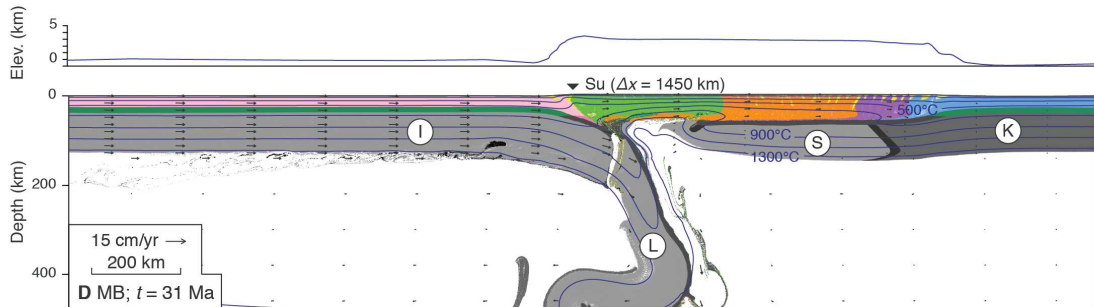
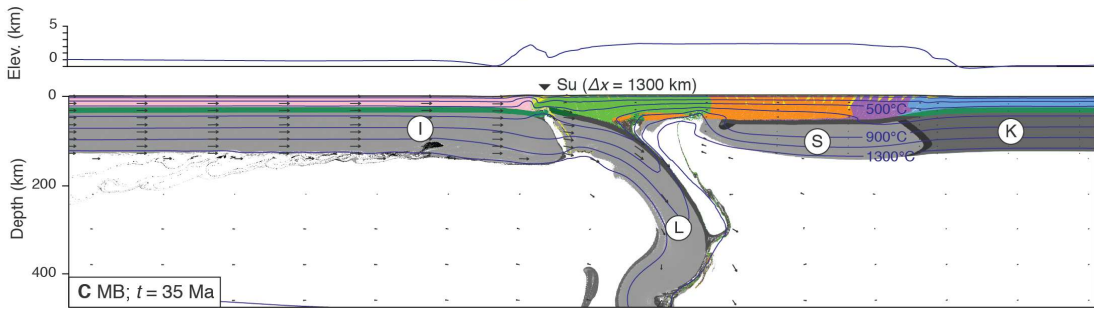
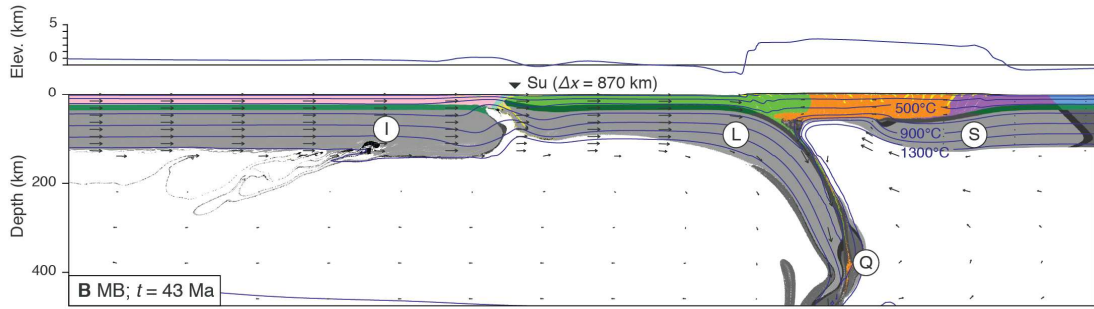
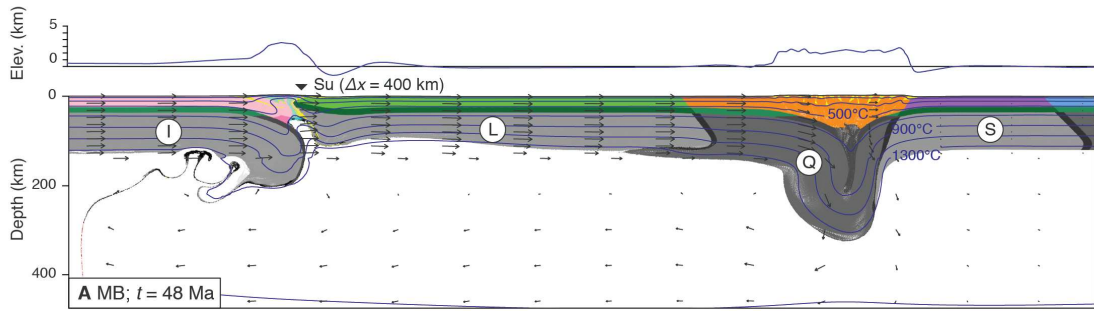


Figure DR1. Evolution of Model MA showing early plateau development in the Q-terrane and subsequent north and south expansion. See Video DR1 for complete annotated evolution.  $\Delta x = \dots$  km is the northward translation of the model IYS suture, Su, since slab breakoff. Note panels are shown in a model window that moves to the right as the model evolves.



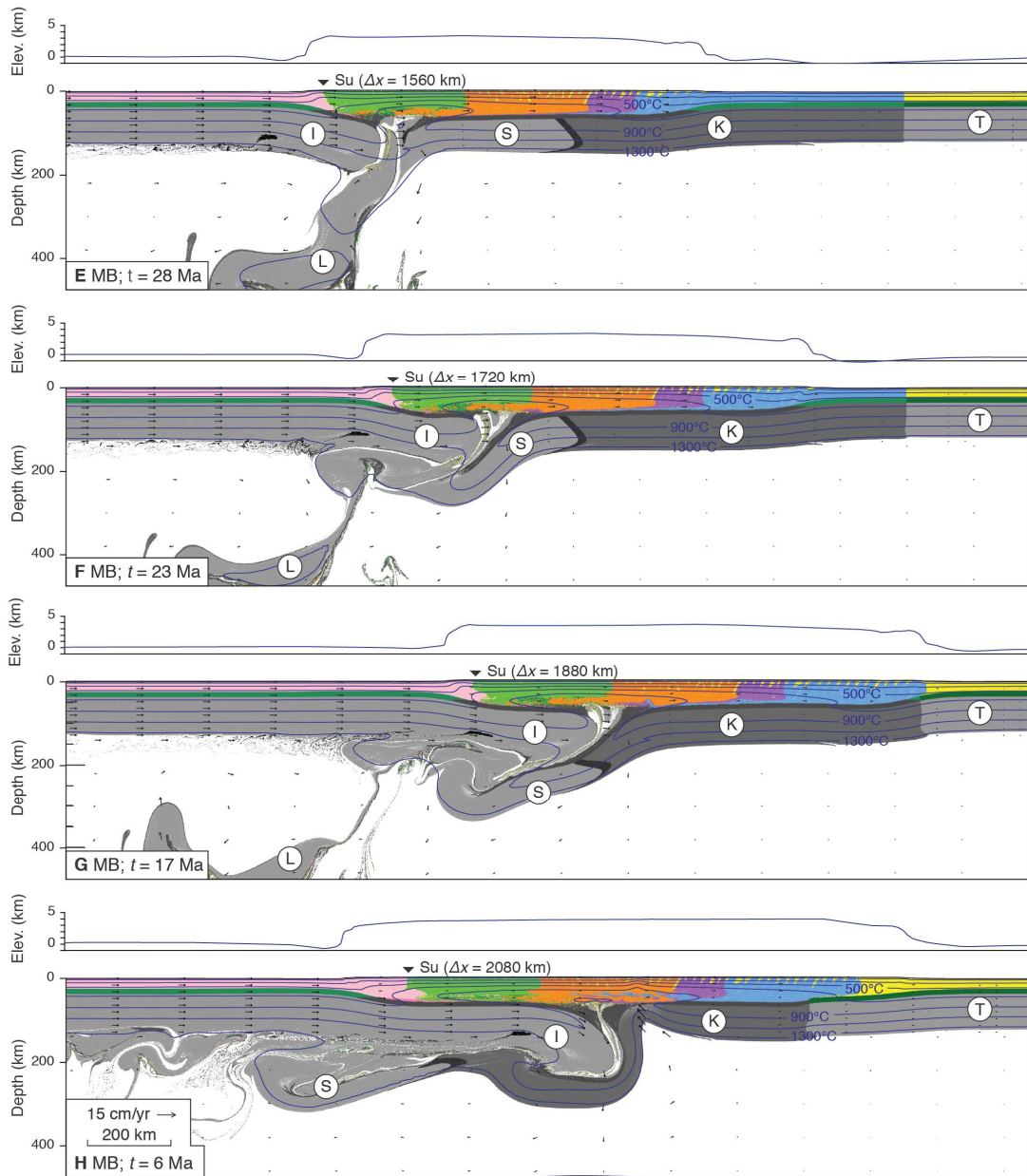


Figure DR2. Evolution of Model MB showing early plateau development in the Q-terrane and subsequent north and south expansion. See Video DR2 for complete annotated evolution.  $\Delta x = \dots \text{km}$  is the northward translation of the model IYS suture, Su, since slab breakoff. Note panels are shown in a model window that moves to the right as the model evolves.

Video DR1 (animation of MA)

2020002\_Video DR1.gif

Video DR2 (animation of MB)

2020002\_Video DR2.gif